Delft University of Technology

Drude Dispersion in the Transmission Line Modeling of Bulk Absorbers at Sub-mm Wave Frequencies
A Tool for Absorber Optimization

van Schelven, Ralph Matthijs; Fiorellini Bernardis, Arturo; Sberna, Paolo; Neto, Andrea

Important note
To cite this publication, please use the final published version (if applicable).
Please check the document version above.

Drude Dispersion in the Transmission Line Modelling of Bulk Absorbers at Sub-mm Wave Frequencies

Ralph M. van Schelven, *Student Member, IEEE*, Arturo Fiorellini Bernardis, Paolo Sberna, Andrea Neto, *Fellow, IEEE*

Abstract— **Semiconductor based bulk absorbers operating in the (sub-) THz range are discussed. The conductivities of the bulk media are described by the Drude model for electron gas where the electron density is controlled. The Drude model predicts the existence of two frequencies of interest, one associated to the scattering time of the electrons, and a second associated to the plasma frequency. The dimensions of absorbers for a specific frequency range can be minimized by tuning the doping levels. Eventually, the maximum ohmic absorption from a bulk material is achieved when the real part of the characteristic impedance of the absorber is matched to the one of the surrounding medium and the imaginary part of the characteristic impedance is high, so that the power entering the material is actually transformed in heat. Using a classic transmission line representation a matching layer is introduced, to further increase the absorbtion capabilities of a semiconductor slab. Measurements using a time domain spectroscopy system show the increased accuracy of the Drude model compared to the quasi-static approximation of the conductivity. The transmission line representation in combination with the Drude model shows to be a simple and accurate tool for integrated antenna front end design and absorber optimization.**

Index Terms—**Absorbers, Characteristic impedance, Drude model, Semiconductors.**

I. Introduction

THE Drude's theory for conduction electrons is a fairly accurate description of the electromagnetic waves dispersion in metals [1], whose typical resisitivity is lower than $10^{-4}\Omega$cm. However, it is not often considered in all its details by the antennas scientific community, since the dependence of the conductivity of metals on frequency starts to become significant at frequencies much higher than the upper limit of the antennas working frequency range (i.e. hundreds of GHz). Indeed, up to 5 THz, metals can be considered very good conductors amenable to the low loss simplifications assumed by Leontovich [2].

On the other hand, for mildly doped semiconductors, whose typical resistivity falls between 1 and 100 Ωcm, the Drude's model predicts a strong frequency dependence of the conductivity and dielectric constant already in the GHz range. The dispersion properties of semiconductors (SCs) were observed with increasing interest since the fabrication of the first Si and Ge devices (diodes, bipolar transistors etc). Later, the first models for the high frequency (> 100 GHz) properties for these devices were developed from the mid-sixties [3]. In particular, the Drude's model was proven to be fundamental for the explanation of the high frequency diode response as

a function of the spreading resistance [4]. Moreover, it was not before 1978 that the high frequency cut-off of Schottky diodes was understood, again thanks to the Drude's theory of free charge carriers in SCs [5].

During the 1990's, significant technological breakthroughs in THz time domain spectroscopy (TDS) [6] allowed the accurate measurement of the SCs free charge carriers scattering time, electrical mobility, and effective mass. The experimental results reported in [6]–[8] demonstrated also that the Drude's model, despite its simplicity, describes these conduction parameters well for SCs, such as Si, in the GHz and THz range. For specific reading, comprehensive reviews on SCs dispersion can be found in [9], [10]. In order to overcome some inaccuracies and limits of the Drude's theory for SCs, numerical approaches, based on Monte Carlo simulations, Maxwell equations and Molecular Dynamics, have been presented in [11]. However, this kind of complex methodologies resulted to be less than 10% more accurate for the determination of the frequency dependent complex conductivity of Si. Hence, the Drude's theory still remains the simplest classical model that can predict the SCs dispersion properties with minimal computational efforts, allowing fast engineering of SC-based components for antenna systems and imagers.

For historical reasons, all the Drudes theory aspects and consequences, widely studied by the physicist and time domain community, have not yet received the proper attention by the microwave and THz engineering community. For example, in the modeling of state of the art of CMOS integrated detectors, of which one pixel could be as shown in Fig. 1, and imaging arrays [12], the material's dielectric constant has been assumed frequency independent. Although for some high resistive materials, such as the material considered in [13], the consequences of assuming the conductivity to be frequency independent, are negligible, for other materials the overestimation of the ohmic losses is very significant [14].

Moreover it appears that SC composites have not been exploited in the design of absorbers yet. Bulk absorbers in the THz regime could be simply fabricated by silicon micromachining and deep reactive ion etching. High resolution imaging in the THz band [12], [15]–[17], is for instance a technological field in which arrays of antenna coupled dielectric lenses are often adopted. Each lens corresponds to a specific observation direction, and the mutual coupling between feeds of different lenses must be avoided. The mutual coupling can be hindered by selectively increasing the conductivity of
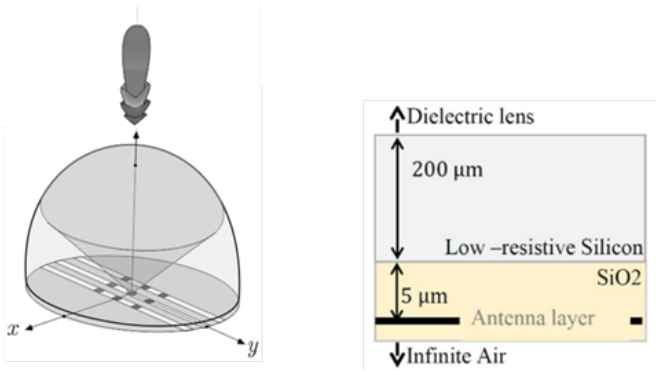
Fig. 1. Example of stratification consisting of an antenna and a dielectric lens, separated by a thin layer of low-resistivity silicon.

Fig. 3. Resistivity of gold as a function of the frequency calculated using the given parameters.
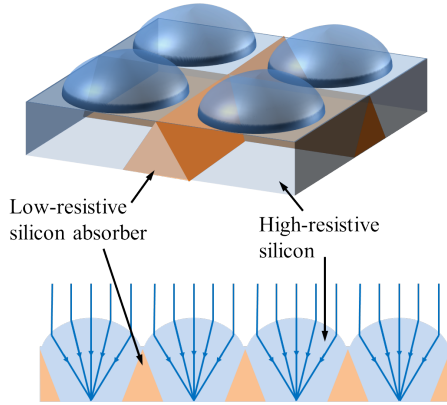

Fig. 2. On-chip lens array made of high resistive silicon. Locally increasing the doping levels for maximum absorption can be used to reduce surface wave propagation in the chip.

specific lateral portions of the lenses to render them opaque, as shown in Fig. 2.

When complying with stringent volume requirements, the fine tuning of the parameters of the SC slabs leads to significant ohmic losses which can be characterized by equivalent transmission lines. These losses imply characteristic impedances whose imaginary part is comparable to the real part. These lines are not usually addressed in the microwave community and they require an heuristic approach to the design as there are no well known design principles.

In this paper we first present a review on the Drude's model for metals and SCs. In the following sections we show how to design SC absorbers employing the Drude's theory together with transmission line model.

This paper is structured follows: in section II we discuss the Drude model in the context of a good conductor, specifically gold. Hereafter, the dispersion of bulk SC materials is considered, by analysing the behaviour of n-doped silicon in section III. The characteristic impedance of the doped silicon is used in this transmission line model and in section IV the dependence of the doping and the frequency behaviour of this characteristic impedance is studied. The model is verified using a TDS system in section V by implementing a transmission line model describing a finite slab of doped
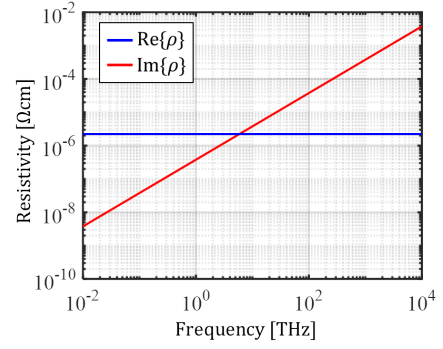
silicon. Section VI describes several applications where the Drude model can be used to improve the accuracy of front end modelling and aid in absorber design. Finally, in section VII the most important findings are summarized and conclusions are drawn.

II. ANALYSIS OF CONDUCTOR USING DRUDE MODEL

The most important characteristics of the Drude model will be briefly summarized in this section, in order to provide the reader with a complete view and to introduce essential variables and terminology used in this article. The effective parameters from the Drude model as a function of the frequency are discussed focusing on bulk metals, specifically gold.

In the quasi-static limit, the conductivity of a metal or a SC can be approximated as

$$\sigma_{qs} = \frac{ne^2\tau}{m_e} \tag{1}$$

where n is the electron density, $e = 1.6 \times 10^{-19}$ C is the charge of an electron and $m_e = 9.1 \times 10^{-31}$ kg is the mass of a free electron. The scattering time, τ, characterizes the electron gas, and in the case of a metal it is in the order of femto seconds (27 fs for gold at room temperature).

The model predicts a linear frequency dependent resistivity as

$$\rho(\omega) = \rho_{qs}(1 + j\omega\tau) \tag{2}$$

where $\rho_{qs} = 1/\sigma_{qs}$ and both σ_{qs} and τ have been provided in (1). As a specific case, the resistivity of gold calculated using the Drude model, at 300 K is shown in Fig. 3. The electron density is $n = 5.9 \times 10^{28}$ electrons/m^3. At very low frequency the resistivity is seen to be mostly real. Drude's model introduces a frequency dependence for the conductivity of the metal, describing the bulk material as an ion sea, with free electrons. The free electrons are accelerated by the presence of an electric field, and hit the metal ions, as shown in Fig. 4. When these hits occur, kinetic energy is transferred to the ions which are accelerated, and as a consequence heat is generated. In a first order approximation the average time, τ, between successive hits of electron and the ion sea, does not depend on the electric field. Instead it depends on the effective scattering surface of the ions, which is a
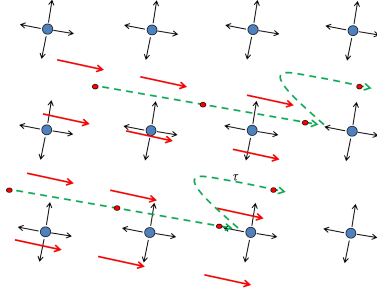
Fig. 4. Free electrons (red dots) are accelerated by a low frequency electric field (red arrows) until they hit a metal ion (blue dots), which is in turn accelerated.
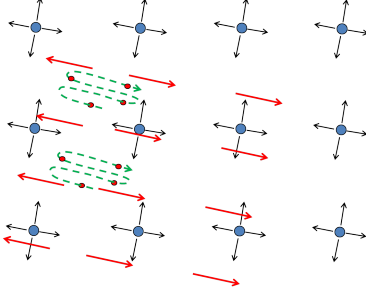

Fig. 5. Free electrons (red dots) are accelerated by a high frequency electric field (red arrows). The direction of the electric field changes sign before the electrons hit an ion (blue dots) and the electrons are oscillating without transferring energy to the ions.

function of the temperature via the average energy of the ions. Significant changes in the resistivity occur as the frequency of the electromagnetic wave propagating in metal increases. At the transition frequency $f = f_\tau = 1/(2\pi\tau)$, which for gold corresponds to 6 THz, the imaginary part of the resistivity becomes as large as the the real part. This corresponds to the notion that for frequencies higher than f_τ, the electric field changes sign with period shorter than τ. Accordingly within the time interval τ the electrons are accelerated in alternating opposite directions. For this reason the electrons do not discharge all the kinetic energy they acquired into the ion sea. A pictorial view of the average electron accelerated by a high frequency electric field is shown in Fig. 5.

From (2) the frequency dependent conductivity is

$$\sigma(\omega) = \frac{\sigma_{qs}}{1 + j\omega\tau} = \frac{\sigma_{qs}}{1 + \omega^2\tau^2} - j\frac{\sigma_{qs}\omega\tau}{1 + \omega^2\tau^2}. \quad (3)$$

The introduction of (3) in Maxwell's equations provides the effective dielectric constant

$$\varepsilon_{\text{eff}}(\omega) = \varepsilon_0\varepsilon_{\text{r,eff}} = \varepsilon_0\varepsilon_{\text{r}\infty}\left(1 - \frac{j\sigma(\omega)}{\omega\varepsilon_{\text{r}\infty}\varepsilon_0}\right). \quad (4)$$

The effective dielectric constant presents both a real and an imaginary part which can be isolated after introducing the plasma frequency as [18]:

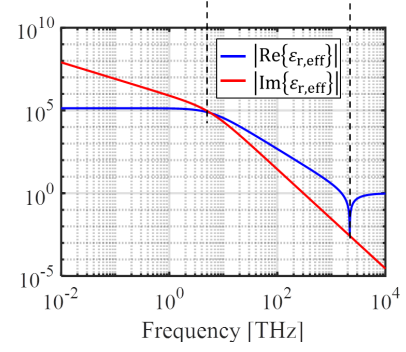$$\omega_p^2 = \frac{ne^2}{\varepsilon_{\text{r}\infty}\varepsilon_0 m_e} \quad (5)$$

Fig. 6. Absolute value of the real and imaginary part of the effective relative permittivity of gold calculated using the given parameters. Both real and Imaginary parts are negative for frequencies lower than the plasma frequency.

one finds

$$\varepsilon_{\text{r,eff}}(\omega) = \varepsilon_{\text{r}\infty}\left[1 - \omega_p^2\tau^2\left(\frac{1}{1 + \omega^2\tau^2}\right)\right] \\ - j\varepsilon_{\text{r}\infty}\omega_p^2\frac{\tau^2}{\tau\omega}\left(\frac{1}{1 + \omega^2\tau^2}\right). \quad (6)$$

The absolute values of the real and imaginary parts of the effective relative dielectric constant are plotted in Fig. 6 again for the case of gold, calculated using the given parameters ($\varepsilon_{\text{r}\infty} = 1$). The term in (6) within square parenthesis expresses the real part of the effective relative dielectric constant. Since for gold at room temperature $\omega_p^2\tau^2 \approx 1.6 \times 10^5$, it is apparent that for frequencies lower than the plasma frequency the real part of the effective dielectric constant is negative.

A similar transition to the one that was observed in the resistivity can be observed in the equivalent relative dielectric constant. For frequencies lower than f_τ the imaginary part of the effective relative dielectric constant is much larger than the real part, and also that at extremely high frequencies ($f > f_p$, $f_p = \omega_p/2\pi$), gold, as all metals, becomes transparent.

The propagation constant also shows a signature associated to the f_τ transition. The propagation constant for gold, calculated using the Drude model, is plotted in Fig. 7 with frequencies varied both in linear and in logarithmic scale. For frequencies below 2200 THz propagation in gold is highly attenuated. However, on an logarithmic scale, it is apparent that from DC to the mentioned $f_\tau = 6$ THz the amplitude of the real part of the propagation constant increases in the same way as the amplitude of the imaginary part. At $f_\tau = 6$ THz the real part of the propagation constant reaches a maximum value and then decreases, while the imaginary part saturates at approximately 20 THz.

The transition that characterizes the propagation and attenuation constant corresponds to the change in the dominant mechanism of attenuation for the EM waves in the metal: at low frequencies there are ohmic losses corresponding to the transformation of EM energy into kinetic energy, while at higher frequencies there is attenuation with minimal phase progression. The electron density in the metal is very high, and as the electrons are excited by an incident wave they radiate a scattered field which opposes the propagation of
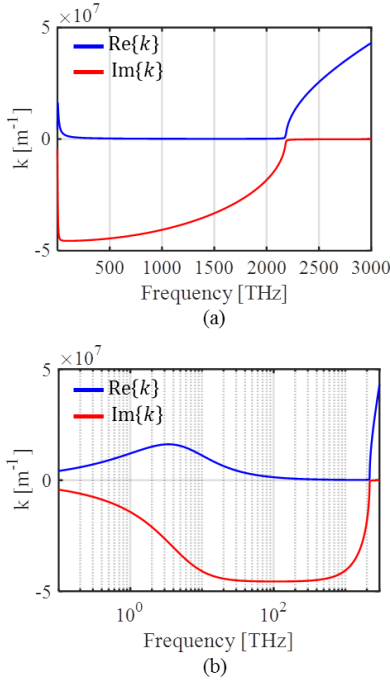
Fig. 7. The propagation constant of an electromagnetic wave within gold, calculated using the given parameters (a) Frequency on a linear scale. (b) Frequency on a logarithmic scale.
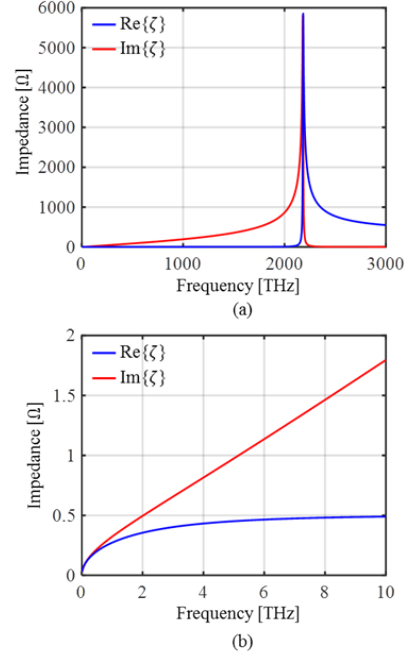

Fig. 8. Characteristic Impedance of gold calculated using the given parameters. (a) Complete spectrum under consideration. (b) Zoomed in on low frequencies.

waves (similarly to what happens in a waveguide in cut-off). As long as the average distances between the electrons are small in terms of the wavelength the scattering interferes destructively with progressive waves in the metal. As the frequency increases, the electrons become too massive to respond with an acceleration to the force impressed by the electric field before this changes sign. Since the electrons are less accelerated, they also do not radiate the scattered field. Therefore, the total field in the metal is only represented by the incident field that can propagate in the metal unobstructed. The specific frequency at which this happens, f_p, depends on the electron density and the effective mass of the electrons.

Mathematically this condition is represented by the real part of the effective dielectric constant rising higher than zero, i.e. $1 - \omega_p^2 \tau^2 / (1 + \omega^2 \tau^2) > 0$, which happens as the frequency increases to values higher than the plasma frequency.

Another interesting parameter is the characteristic impedance of the gold calculated using the Drude model, which is shown in Fig. 8. The impedance tends to $\zeta_0 \approx 377\,\Omega$ for frequencies much higher than the plasma frequency of the metal, it undergoes a resonance at the plasma frequency, and it is mostly imaginary for lower frequencies. However, a zoomed view at the impedance curves at low frequencies, Fig. 8(b), shows that for frequencies below 1 THz the real and imaginary parts of the impedance tend to be equal. The fact that real and imaginary parts have the same value is the signature of the "good conductor" behaviour on which the Leontovich [2] approximation for losses is built.

III. SEMICONDUCTOR DISPERSION

Also for doped bulk SC materials the quasi static conductivity can be approximated using (1). Here we are neglecting the hole conductivity, which is in fact neglicable for n-doped SC materials. For SCs an equivalent electron mass is used to account for the diminished inertia of electrons embedded in a periodic lattice potential: $m_{e,si} = 0.29 m_e$ for silicon (Si) [6]. The scattering time τ for silicon is in the order of few pico seconds, depending on the doping, and the temperature. The scattering time is found as

$$\tau = \frac{m_{si}}{e}\mu \tag{7}$$

where the mobility μ is at $T = 300$ K equal to [19]

$$\mu = \mu_{min} + \frac{\mu_{max} - \mu_{min}}{1 + (n/N_{ref,1})^{\alpha_1}} - \frac{\mu_1}{1 + (N_{ref,2}/n)^{\alpha_2}} \tag{8}$$

The several parameters in (8) are based on experimental data and the values are: $\mu_{min} = 6.85 \times 10^{-3}$ m^{2}V^{-1}s^{-1}, $\mu_{max} = 0.1414$ m^{2}V^{-1}s^{-1}, $\mu_1 = 5.61 \times 10^{-3}$ m^{2}V^{-1}s^{-1}, $N_{ref,1} = 9.20 \times 10^{22}$ m^{-3}, $N_{ref,2} = 3.41 \times 10^{26}$ m^{-3}, $\alpha_1 = 0.711$ and $\alpha_2 = 1.98$. For SC materials the transition frequencies, f_τ are in the few hundreds of GHz ranges. Also the plasma frequencies can be in this frequency range depending on the doping levels. Therefore both these frequencies should be reason for attention specifically for mm- and sub-mm wave front end designers.

Similar as to the case of gold, the effective relative permittivity of the SC can be calculated as a function of frequency from the Drude model using (6), so that the characteristic impedance of the SC and its propagation constant are expressed as $\zeta = \zeta_0 / \sqrt{\varepsilon_{r,eff}}$ and $k = k_0 \sqrt{\varepsilon_{r,eff}}$ respectively. Fig-
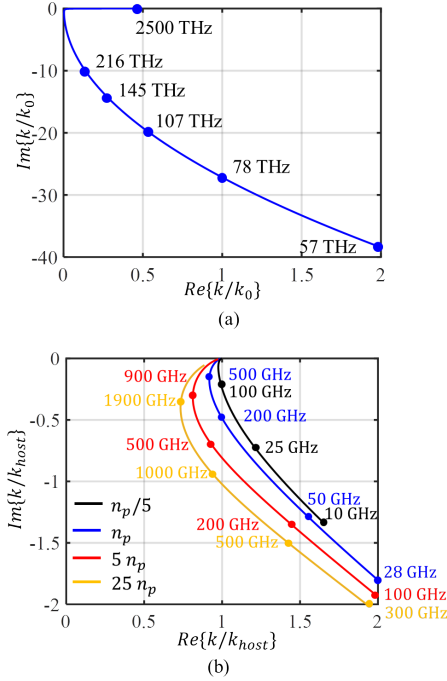
(a)

(b)

Fig. 9. Dispersion of the propagation constant,calculated using the given parameters, in the complex plane. (a) In the case of gold. (b) In the case of semiconductors with varying doping levels. Several frequency points along the different curves are indicated.

(a)

(b)

Fig. 10. (a) Resistivity of doped silicon ($n_p = 8.8 \times 10^{21} \mathrm{m}^{-3}$), calculated using the given parameters, as a function of frequency. (b) Characteristic impedance of doped silicon, calculated using the given parameters, for three different levels of doping. Also the plasma frequencies are indicated.

ure 9 shows the dispersion curves of plane waves propagating in gold (Fig. 9(a)) and in doped silicon (Fig. 9(b)), calculated using the Drude model and the appropriate parameter values. The propagation constants normalized to propagation constant of free space, k_0, (for gold) and to the propagation constant of undoped silicon, $k_{\mathrm{host}} = k_0\sqrt{\varepsilon_{\mathrm{r\infty}}}$, (for the silicon), are shown as functions of the frequency. The propagation constant of gold undergoes a very drastic transition after $f_p = 2200$ THz, as for frequencies higher than f_p, waves are actually allowed to propagate without significant attenuation. The case of silicon presents a more complex dispersion. The plasma frequency in SCs depends largely on the doping levels, and accordingly the dispersive properties can be designed to meet certain requirements. In the case shown in Fig. 9(b) four different levels of doping are considered. The parametrization is referred to $n = n_p = (\varepsilon_{\mathrm{r\infty}}\varepsilon_0 m_{e,si})/(\tau_{si}^2 e^2) = 8.8 \times 10^{21}$ m^{-3}. This doping is such that $f_p = f_\tau$ and corresponds to $\rho_{qs} = 0.6\Omega$cm. These orders of doping levels are common in silicon wafers used in electronic circuits. The dopings of Fig. 9(b) correspond to $n = n_p/5$, $n = n_p$, $n = 5n_p$ and $n = 25n_p$. The lower doping levels imply lower dispersion, however for higher dopings the frequency dependence of the propagation constant is stronger. From this figure one can anticipate that significant freedom in the design of front ends at (sub-) THz frequencies can be obtained by finely controlling the electron doping levels in silicon.

IV. Impedances of Low Resistivity Silicon

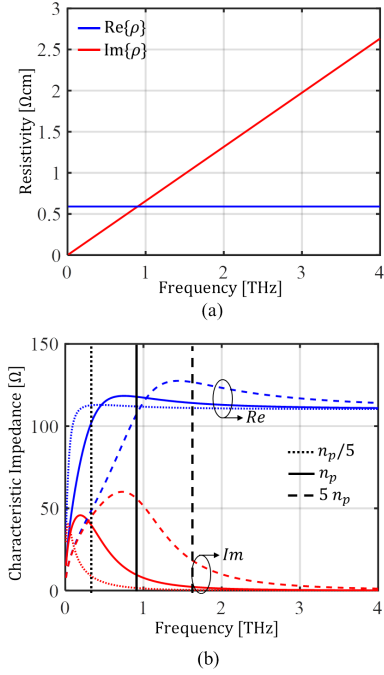Arguably the most important property of a material for an EM engineer is its characteristic impedance. It relates the electric- and magnetic field of a plane wave travelling in a bulk medium, and is routinely introduced in transmission line tools to describe the interaction of waves with the finiteness of the structures. The superposition of multiple reflections in slabs is well understood in the TDS community [6], however, the representation of the total fields via equivalent transmission lines is much less common than in the electrical engineering community. For this reason, to the authors knowledge, the characteristic impedance of a bulk SC cannot be found in published literature.

The resistivity of doped silicon, as calculated using the Drude model, with $n = n_p$ is shown in Fig 10(a). The same behaviour as for the resisitivity of gold is seen, where the real part is constant as a function of the frequency while the imaginary part grows linearly, reaching the value of the real part at f_τ. The characteristic impedance of silicon doped with different electron densities is shown in Fig. 10(b). The characteristic impedance of doped silicon is

$$\zeta(\omega) = \frac{\zeta_0}{\sqrt{\varepsilon_{r,eff}(\omega)}} \tag{9}$$

where $\varepsilon_{r,eff}(\omega)$ is introduced in (6). After some algebraic steps (9) is written as

$$\zeta(\omega) = e^{j\pi/4}\sqrt{\frac{\mu_0\omega}{\sigma_{qs}}}\sqrt{\frac{1 + \omega^2\tau^2}{1 + j\gamma(\omega)}} \tag{10}$$

where we introduced

$$\gamma(\omega) = \frac{\omega}{\omega_p^2\tau}\left(1 + (\omega^2 - \omega_p^2)\tau^2\right). \tag{11}$$

In the limit for low frequency it can be seen that γ goes to zero, so that

$$\zeta(\omega \ll \omega_p) = \sqrt{\frac{\mu_0 \omega}{2\sigma_{qs}}}(1+j) \qquad (12)$$

which is recognized as the leontovich approximation for good conductors. Instead, for very high frequencies (i.e. $\omega \gg \omega_p$), using $\omega_p^2 \tau = \sigma_{qs}/(\varepsilon_{r\infty}\varepsilon_0)$, we see

$$\gamma(\omega \gg \omega_p) = \frac{\omega \varepsilon_{r\infty}\varepsilon_0}{\sigma_{qs}}\left(1+\omega^2\tau^2\right) \qquad (13)$$

so that

$$\zeta(\omega \gg \omega_p) = \sqrt{\frac{\mu_0}{\varepsilon_{r\infty}\varepsilon_0}}. \qquad (14)$$

The impedance behaviour in the frequency range around ω_p shows an interesting behaviour. As the frequency grows from very low frequency, both real and imaginary parts, R_{Si} and X_{Si} respectively, of the impedance rise and show a peak close to each other in frequency. In Sec. VI it will be shown that the percentage of incident power absorbed within the SC is maximal at a frequency between the peaks of R_{Si} and X_{Si}.

A better physical understanding of the imaginary part can be understood as follows. Assuming a plane wave to propagate in positive z-direction and the magnetic field to be of zero phase at a given observation point, the corresponding electric field is

$$\overrightarrow{e} = \zeta \overrightarrow{h} \times \hat{z} = (R_{Si} + jX_{Si})\overrightarrow{h} \times \hat{z}, \qquad (15)$$

which presents two components that are $90°$ phase shifted. One component is in phase with the magnetic field, $\overrightarrow{e} = R_{Si}\overrightarrow{h} \times \hat{z}$, and thus contributes to the real part of the pointing vector along $\hat{z}$ as

$$Re\{S_z\} = \frac{1}{2}R_{Si}|\overrightarrow{h}|^2. \qquad (16)$$

The second component is in quadrature to the magnetic field: $\overrightarrow{e} = jX_{Si}\overrightarrow{h} \times \hat{z}$. This term contributes only to reactive energy transported in the longitudinal direction. However, this same component of the electric field is actually in phase with the flow of electrons in the silicon (electric currents) and thus directly contributes to losses. The imaginary part of the characteristic impedance is associated to real power in the form of ohmic losses. It can observed from Fig. 10 that for increasing frequency, the value of R_{Si} tends to the impedance in absence of doping, while X_{Si} decreases, resulting in lower ohmic losses with frequency.

V. VERIFICATION OF THE MODEL

The Drude model for the dispersion of the semi-conductors in (6) had first been validated in [6]. In this section we present an experimental validation that largely follows the one in [6], by means of state of the art TDS measurement equipment [20] and silicon wafers.

The experiment was conducted in the following way. Two photoconductive antennas face each other and are coupled by means of a quasi-optical path consisting of four spherical lenses that focus the field radiated by the transmitting (TX) antenna onto the receiving (RX) one. The antennas are excited
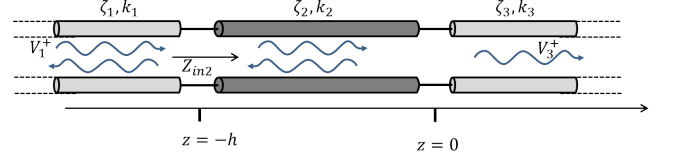

Fig. 11. Transmission line model representing the absorbing slab surrounded by a lossless host medium.

by a pulsed in-fiber gaussian laser at 1580 nm, each pulse having a full width at half maximum of 100 fs and being repeated at 100 MHz. The TX antenna is biased to a constant voltage, $V_b = 100$ V, that accelerates the carriers injected by the laser generating the radiating process; the carriers freed in the RX antenna are accelerated by the incoming THz radiation. The Si wafer is positioned in the middle of the quasi-optical path, and the time-domain current induced in the RX antenna is sampled and its spectrum calculated. The spectrum of the induced current on the receiving antenna is calculated both with and without the sample in the quasi-optical path. From these spectra the dielectric properties of the slab can be extrapolated, by knowing its geometry and location.

In the following we consider a SC slab, that is much larger in the transverse directions, i.e. the x- and y-directions, than the width of the beam profile generated by the TDS system. The slab has a finite thickness, h, in z-direction and it is surrounded above and below by free space. The beam profiles can be represented as normally incident plane waves. Thus the total electric field can be expressed as the product of a voltage, V, and a transverse normalized field unit vector, $\hat{e}_t$

$$\overrightarrow{E}_t(\overrightarrow{r}) = V(z)\hat{e}_t. \qquad (17)$$

Resorting to a standard transmission line representation, as shown in Fig. 11, the voltage distributions in the slab (medium 2) and in the two half spaces of host material (free space in this case) for $z < -h$ (medium 1) and and $z > 0$ (medium 3) can be expressed as the superpositions of incident and reflected waves

$$V_i(z) = V_i^+ e^{-jk_i z} + V_i^- e^{jk_i z} \qquad (18)$$

where the subscript $i = 1, 2, 3$ indicates the portion of space under consideration. The propagation constant and the characteristic impedance of the transmission lines in Fig. 11 are those of the host material for medium 1 and 3, and those of SC material for medium 2.

After a few algebraic steps, the transmission line solution for the value of the voltage propagating after the slab to the receiver of the measurement setup is

$$V_3^+ = V_2^+(1 + \Gamma_{\text{in}}) = V_1^+ \frac{e^{jk_1 h}(1 + \Gamma_{\text{in}})(1 + \Gamma_{\text{out}})}{e^{jk_2 h} + \Gamma_{\text{out}}e^{-jk_2 h}} \qquad (19)$$

where $\Gamma_{\text{in}} = (Z_{in2} - \zeta_{\text{host}})/(Z_{in2} + \zeta_{\text{host}})$ and $\Gamma_{\text{out}} = (\zeta_{\text{host}} - \zeta)/(\zeta_{\text{host}} + \zeta)$ are the voltage reflection coefficients at the cross sections $z = -h$ and $z = 0$ respectively.

Figure 12 presents the amplitude of the transmission coefficient, $T = V_3^+/V_1^+$ as a function of the frequency for a dielectric slab of silicon of thickness $h = 434\mu$m and
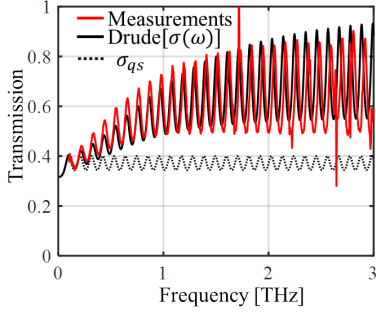
Fig. 12. Transmission through a slab of doped silicon. $h = 434\,\mu$m, $n = 1.16 \times 10^{21}\,\text{m}^{-3}$. A comparison between measurements, the Drude model and the quasi static approximation is shown.

resistivity declared by the provider of $5\,\Omega$cm. The value of $\varepsilon_{r,\infty}$ of the slab is found beforehand to be 10.5. In the model a nominal resistivity of $\rho_{qs} = 3.77\,\Omega$cm corresponding to a doping of $n = 1.16 \times 10^{21}$ was adopted because it led to the best fit. The scattering time is found using (7). It is apparent that the frequency independent nominal resistivity, or conductivity, does not represent the losses in the dielectric slab for frequencies higher than a few hundred GHz. Meanwhile the transmission coefficient evaluated via the full Drude model and the measured one show very good agreement within the measurement accuracy. The expected and measured oscillations are directly related to the multiple reflections at the dielectric air interfaces.

From the same measurements, the TDS measurement equipment [20] allows to extract the index of refraction ($\sqrt{\varepsilon_{r,\text{eff}}}$). In Fig. 13 the measured real and imaginary parts (red solid curves) are compared with the ones predicted by the Drude model (black solid lines), and a model that only considers the quasi static, frequency independent, approximation for the conductivity (dashed lines). It is apparent that the accuracy of the measured $Im\{\sqrt{\varepsilon_{r,\text{eff}}}\}$ (proportional to the attenuation constant) is impacted by the multiple reflections within the slab. On the large scale of Fig. 13 (a) both models seem to agree very well with measurements. However Fig. 13 (b-d) show expanded views of the imaginary part of the index of refraction on separate frequency ranges. The larger apparent dispersions occur at lower frequencies, with $Im\{\sqrt{\varepsilon_{r,\text{eff}}}\}$ varying from -0.7 to -0.1 in the band from 100 GHz to 500 GHz. However in that frequency range, the quasi static approximation of the conductivity already provides $Im\{\sqrt{\varepsilon_{r,\text{eff}}}\}$ with a good accuracy with respect to the measurements and the Drude model. In the frequency range between 0.5 THz to 1.5 THz the measured $Im\{\sqrt{\varepsilon_{r,\text{eff}}}\}$ and the one predicted by the Drude model start to deviate significantly from the one predicted by the quasi static conductivity model. Finally in the ranges from 1.5 THz to 4 THz the $Im\{\sqrt{\varepsilon_{r,\text{eff}}}\}$ is 5 to 20 times smaller than the one predicted by the quasi static conductance approximation, indicating that the full Drude model must be used to assess the losses in doped semiconductors to maintain a useful estimation of the propagation losses. Overall the Drude model captures the dominant features very well, validating the analysis from the previous sections.
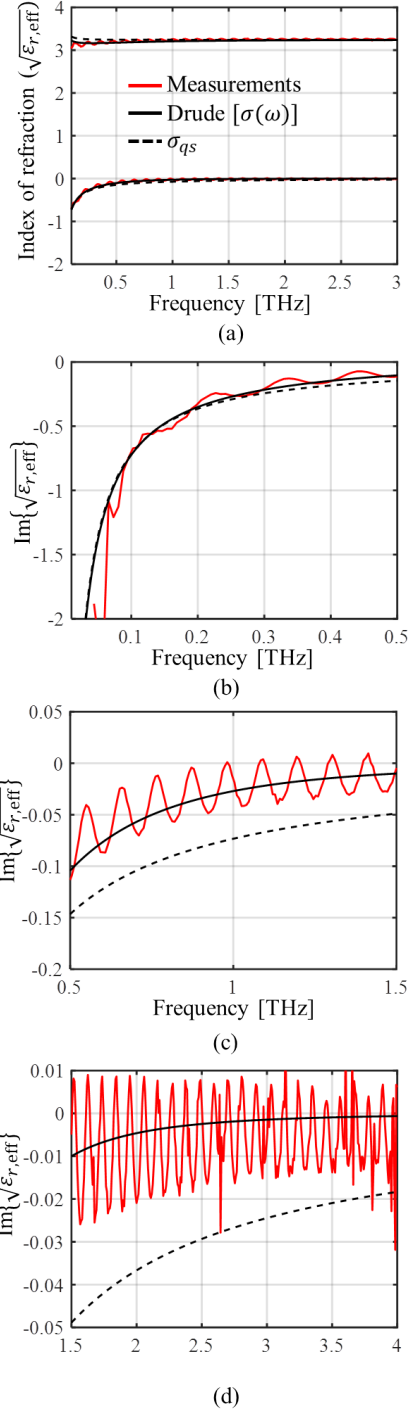

(a)

(b)

(c)

(d)

Fig. 13. Index of refraction of the silicon slab with $h = 434\mu$m, $n = 1.16 \times 10^{21}\,\text{m}^{-3}$. (a) Wide frequency range. (b-d) Zoomed on specific frequency regions.

VI. APPLICATIONS IN ABSORBERS AND LENS DESIGN

In Sec. I integrated lens arrays for imagers were introduced as a typical field of applications where the Drude model is commonly overlooked while estimating the losses. In this section numerical examples will be described to highlight the usefulness of adopting the Drude model in the design stages of integrated lens antennas and absorber design.

In the previous section, it is shown that the transmission line model from Fig. 11 can be used to estimate the power absorbed in a slab of finite thickness surrounded by free space. Here we will consider a slab of doped silicon embedded in both non-doped silicon and free space as examples. The absorbed power in the slab can be expressed as

$$P_{abs} = \frac{1}{2} \iiint_{V_{SC}} Re\{\sigma\} |\overrightarrow{E}_2(x,y,z)|^2 dV \qquad (20)$$

where V_{SC} is the volume of the SC slab and $\overrightarrow{E}_2$ is the electric field inside the slab. The integral can be evaluated analytically as:

$$P_{abs} = \frac{Re\{\sigma\}A}{2} |V_2^+|^2 \frac{1}{2\alpha} \left(e^{2\alpha h} - 1 + |\Gamma_{out}|^2 (1 - e^{-2\alpha h}) \right) \qquad (21)$$

where σ is provided in (3), $\alpha = -Im\{k_2\}$ and A is the effective area under illumination. The effective area under illumination is only needed to provide absolute power values. However if the absorbed power is normalized to the incident power,

$$P_{inc} = \frac{1}{2} \frac{A}{\zeta_{host}} |V_1^+|^2, \qquad (22)$$

the effective area information cancels out.

A. Absorbing slab surrounded by silicon

Using the transmission line model from Fig. 11 and (21) and (22) one can calculate the losses associated to the low resistive silicon layer in the front end design introduced in Fig. 1 [14]. The frequency band under consideration is from 200 to 600 GHz, the thickness of the slab is 200μm and the quasi-static resistivity is $10\,\Omega$cm. This resistivity corresponds to a doping level of $n = 4.5 \times 10^{20}\,$m^{-3}. From the quasi-static approximation, the expected losses over the frequency band of interest are constant slightly below 1 dB. However, after implementing the Drude model it is seen that the losses actually peak at 200 GHz at 1 dB before decreasing with frequency to only 0.6 dB at 600 GHz and lower still at higher frequencies. The losses as a function of frequency calculated using both models are shown in Fig. 14. From Fig. 14 it is clear that the commonly used quasi-static approximation for the conductivity severely overestimates the losses at higher frequencies for the transmission of a wave through low resistive silicon. The lower losses, as calculated from the Drude model, show greater promise for the integration of antennas in low resistive silicon just below silicon lenses at THz frequencies.

The doping level can be tuned to maximize absorption: the highest absorbing efficiency is achieved by the thinnest slab that absorbs the maximum power for a given frequency. Assuming a frequency band centered around a given central frequency, such an SC absorber can be synthesized parametrically by tuning the electron doping, n, and the thickness, h. A good absorber will be the one that

1) Minimizes reflections of the incident waves, i.e. one for which $\zeta_{SC} \approx \zeta_{host}$.
2) Maximizes resistive wave attenuation.

As previously introduced, three frequency regimes, $f < f_\tau$, $f_\tau < f < f_p$ and $f > f_p$, can be identified from the Drude
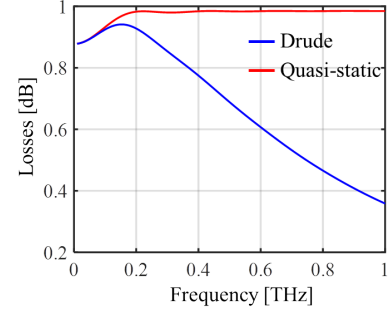

Fig. 14. Losses in a slab of $200\,\mu$m with $\rho_{qs} = 10\,\Omega$cm ($n = 4.5 \times 10^{20}\,$m^{-3}). The expected losses are shown as calculated using the quasi-static approximation and the Drude model.
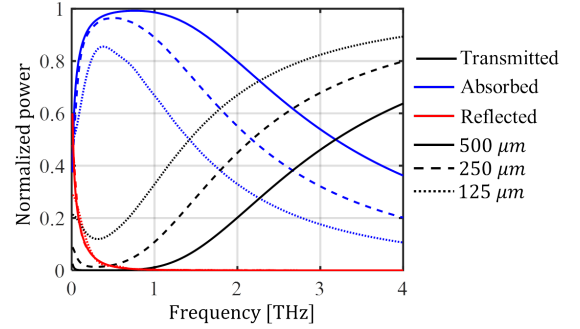

Fig. 15. Calculated normalized transmitted, absorbed and reflected power in a doped silicon slab ($n = n_p = 8.8 \times 10^{21}$, $\rho = 0.6\,\Omega$cm) surrounded by non-doped silicon. Three different slab heights are considered.

model. For frequencies below f_p the real part of the effective dielectric constant is smaller than zero. For frequencies that are also lower than f_τ, waves can still propagate in the SC, with attenuation constant equal to the propagation constant. However, for frequencies in the range $f_\tau < f < f_p$, there is no propagation possible, with or without attenuation. Accordingly the frequencies between the f_τ and f_p are less useful for an efficient absorber. It is apparent that for SC absorbers f_p is a design parameter since the doping n can be finely tuned in a cleanroom environment. Accordingly a starting point for our SC absorber design will be the choice of an electron density doping that cuts out the middle frequencies region, which is achieved by choosing $n = n_p$.

Looking at the absorption within slabs of different thicknesses, as shown in Fig. 15, it is apparent that for $n = n_p$ a slab with thickness of one effective wavelength at 350GHz, corresponding to approximately $250\,\mu$m, is sufficient to absorb over 90% of the incident power. As expected, thicker and thinner slabs absorb a larger and smaller portion of the incident power respectively. Figure 16 shows the power absorbed by a slab of thickness $h = 250\,\mu$m as a function of the frequency and doping level. Lower dopings lead to lower impedance contrasts associated to a lower X_{Si}, however this also implies lower ohmic attenuations. On the other hand, higher dopings lead to higher attenuation per unit length, but also higher reflection at the interfaces.
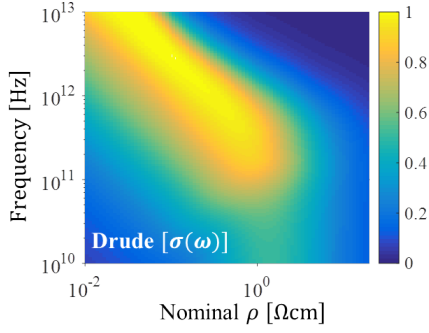
Fig. 16. Normalized absorbed power in a slab of doped silicon, $h = 250\,\mu$m, as a function of both the doping and the frequency calculated using the Drude model.
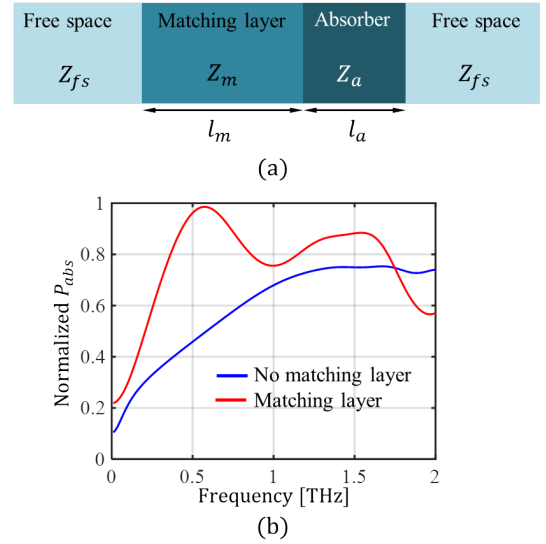

Fig. 17. (a) Densely doped silicon absorber with a matching layer surrounded by free space. (b) Absorbed power in the structure normalized to total incident power for the cases with ($l_m = 81\,\mu$m, $l_a = 44\,\mu$m) and without matching layer ($l_a = 125\,\mu$m). The remaining parameters are: $n = 6n_p = 5.3 \times 10^{22}\,$m^{-3}, $\varepsilon_{r,m} = 3.4$, $n_m = 3 \times 10^{21}\,$m^{-3}.

B. Absorbing slab surrounded by free space

A more clear example of the usefulness of the transmission line representation for the propagation in SC material, involves minimizing the volume of a SC stratification to absorb a wave incident from free space. In this case a silicon with higher doping level, $n = 6n_p = 5.3 \times 10^{22}\,$m^{-3}, is chosen for the main absorber. The power absorbed in this single slab absorber of thickness $125\,\mu$m, is shown in Fig 17, with the maximum absorption being 75% around 1.5 THz. However the introduction of a second perforated doped silicon matching layer can be used to facilitate the penetration from free space to the densely doped silicon. The effective dielectric permittivity of the matching layer in the absence of doping is $\varepsilon_{r,m} = \sqrt{\varepsilon_{r\infty}} = 3.4$. In this second case the matching layer is taken with $l_m = 81\,\mu$m $= \lambda_d/4$ at 500 GHz, where λ_d is the wavelength in the matching layer. The thickness of the core absorber is reduced to $l_a = 44\mu$m, so that the total absorbing thickness remains $125\,\mu$m. The doping level of the matching layer was chosen to be $n_m = 3 \times 10^{21}\,$m^{-3}. In this second case over 95% of the power is absorbed in the cumulative space of $\lambda_0/5$ at 500 GHz. It is interesting to observe that despite the heavy losses in the matching layer, the standard quarter wavelength transformation rule still roughly applies.

VII. Conclusions

The frequency dependent properties of gold and doped silicon are investigated using the Drude model. The propagation constant of bulk silicon for different levels of n-type dopings is presented. The characteristic impedance for low resistivity silicon is also introduced and used in a classic transmission line tool. Here the notable feature is that this tool is used as in standard microwave designs, also in the presence of very high losses per wavelength. By means of time domain sensing measurements the model is validated. It is found that the commonly used quasi static approximation for the conductivity is valid for frequency regimes up to a few hundred GHz. However, for frequencies higher than 300 GHz the Drude model shows significantly more accurate results than the quasi static model compared to measurements.

Guidelines are presented for the synthesis of efficient THz absorbers for a given target frequency, by finely tuning the doping of semiconducting materials. By introducing a matching layer, an absorption of over 95% of the incident power is realized in a slab of one fifth of the wavelength in free space. As the frequency increases above the target frequency, the absorption decreases and the losses in the doped silicon are much lower than would be assumed from the quasi static conductance model.

References

[1] P. Drude, "Zur Elektronentheorie der Metalle", *Annalen der Physik*, Vol. 306, pp. 566613, Mar. 1900

[2] M. A. Leontovich, "Approximate boundary conditions for electromagnetic fields at the surface of a highly conducting body," *Issledovaniyapo Rasprostraneniyu Radiovoln*, Moscow, 1948, pt. 2, pp. 512.

[3] K.S. Champlin, D. B. Armstrong, and P. D. Gunderson. "Charge carrier inertia in semiconductors," *Proceedings of the IEEE* Vol. 52, No. 6, pp. 677-685, 1964.

[4] L.E. Dickens, "Spreading Resistance as a Function of Frequency," *IEEE Transactions on Microwave Theory and Techniques*, Vol. 15, No. 2, pp. 101-109, Feb 1967

[5] K.S. Champlin, and G. Eisenstein, "Cutoff frequency of submillimeter Schottky-barrier diodes," *IEEE Transactions on Microwave Theory and Techniques*, Vol. 26, No. 1, pp. 31-34, 1978

[6] M. van Exter, D. Grischkowsky. "Carrier Dynamics of electrons and holes in moderately doped silicon", *Phys. Rev. B*, vol. 41, no. 17, pp. 12140-12149, June 1990.

[7] Tae-In Jeon and D. Grischkowsky, "Characterization of optically dense, doped semiconductors by reflection THz time domain spectroscopy", *Applied Physics Letters* Volume 72, Number 23, 8 June 1998

[8] Nashima, S., et al. "Measurement of optical properties of highly doped silicon by terahertz time domain reflection spectroscopy." Applied physics letters 79.24 (2001): 3923-3925.

[9] M. Dressel, G. Grner "Electrodynamics of Solids: Optical Properties of Electrons in Matter" Publisher: Cambridge University Press, Year: 2002

[10] M. Dressel, M. Scheffler, "Verifying the Drude response", *Annalen der Physik*, 15, No. 78): 535544. 2006. DOI:10.1002/andp.200510198.

[11] Willis, K. J., S. C. Hagness, and I. Knezevic. "A generalized Drude model for doped silicon at terahertz frequencies derived from microscopic transport simulation." Applied Physics Letters 102.12 (2013): 122113.

[12] R. Al Hadi, H. Sherry, J. Grzyb, Y. Zhao, W. Forster, H. M. Keller, A. Cathelin, A. Kaiser and U. R. Pfeiffer, "A 1 k-Pixel Video Camera for 0.7-1.1 Terahertz Imaging Applications in 65-nm CMOS," *IEEE Journal of Solid-State Circuits*, vol. 47, no. 12, pp. 2999-3012, Dec. 2012

[13] J. Grzyb, K. Statnikov, N. Sarmah, B. Heinemann and U. R. Pfeiffer, "A 210270-GHz Circularly Polarized FMCW Radar With a Single-Lens-Coupled SiGe HBT Chip," *IEEE Trans. Terahertz Science and Technology*, vol. 6, no. 6, pp. 771-783, Nov. 2016

[14] S. L. van Berkel et al., "A Double Leaky Slot Antenna for Wideband THz Direct Detection in CMOS Technology" *Accepted for publication in IEEE Transactions on Terahertz Science and Technology and available as preprint on IEEExplore*.

[15] S. J. C. Yates et al., "Surface Wave Control for Large Arrays of Microwave Kinetic Inductance Detectors," *IEEE Transactions on Terahertz Science and Technology*, vol. 7, no. 6, pp. 789-799, Nov. 2017.

[16] S. van Berkel, O. Yurduseven, A. Freni, A. Neto and N. Llombart, "THz Imaging Using Uncooled Wideband Direct Detection Focal Plane Arrays," *IEEE Transactions on Terahertz Science and Technology*, vol. 7, no. 5, pp. 481-492, Sept. 2017.

[17] S.Bosma, M.Alonso-delPino, C.Jung-Kubiak, D.Blanco, and N.Llombart, "Scanning Lens Phased Array For Submillimeter Wavelengths," in IRMMW, Paris, 2019

[18] Ramo, Whinnery, Duzer, "Fields and waves in Communication Electronics", John Wiley and Sons, 1990

[19] D. B. M. Klaasen, "A Unified Mobility Model for Device Simulation - I. Model Equations and Concentration Dependence," *Solid State Electronics*, vol. 35, no. 7, pp. 953-959, 1992.

[20] Menlo Systems (https://www.menlosystems.com/products/thz-time-domain-solutions/terak15-terahertz-spectrometer/)